nature protocols

PROTOCOL

https://doi.org/10.1038/s41596-020-00487-w

Check for updates

Snapshot photoacoustic topography through an ergodic relay of optical absorption in vivo

Lei Li[1,2], Yang Li[1,2], Yide Zhang[1] and Lihong V. Wang[1]✉

Photoacoustic tomography (PAT) has demonstrated versatile biomedical applications, ranging from tracking single cells to monitoring whole-body dynamics of small animals and diagnosing human breast cancer. Currently, PAT has two major implementations: photoacoustic computed tomography (PACT) and photoacoustic microscopy (PAM). PACT uses a multi-element ultrasonic array for parallel detection, which is relatively complex and expensive. In contrast, PAM requires point-by-point scanning with a single-element detector, which has a limited imaging throughput. The trade-off between the system cost and throughput demands a new imaging method. To this end, we have developed photoacoustic topography through an ergodic relay (PATER). PATER can capture a wide-field image with only a single-element ultrasonic detector upon a single laser shot. This protocol describes the detailed procedures for PATER system construction, including component selection, equipment setup and system alignment. A step-by-step guide for in vivo imaging of a mouse brain is provided as an example application. Data acquisition, image reconstruction and troubleshooting procedures are also elaborated. It takes ~130 min to carry out this protocol, including ~60 min for both calibration and snapshot wide-field data acquisition using a laser with a 2-kHz pulse repetition rate. PATER offers low-cost snapshot wide-field imaging of fast dynamics, such as visualizing blood pulse wave propagation and tracking melanoma tumor cell circulation in mice in vivo. We envision that PATER will have wide biomedical applications and anticipate that the compact size of the setup will allow it to be further developed as a wearable device to monitor human vital signs.

Introduction

Photoacoustic tomography (PAT), also known as optoacoustic tomography, is a noninvasive hybrid imaging technology that combines the power to image with high spatial resolution inside deep tissue by using ultrasound with the molecular contrast of optical imaging[1–3]. Capitalizing on the photoacoustic (PA) effect, in PAT, the optical energy is absorbed by chromophores in the biological tissue and re-emitted as ultrasonic waves (referred to as PA waves)[4,5]. By detecting the PA waves, tomographic images with optical contrasts can be generated[6,7]. Taking advantage of the weak scattering of ultrasound in soft tissue, PAT achieves superb resolution at depths up to several centimeters[8]. Currently, PAT has two major implementations based on the image-formation method: inverse reconstruction–based photoacoustic computed tomography (PACT) and focus-scanning–based photoacoustic microscopy (PAM)[9,10]. By usinging a multi-element ultrasonic array, PACT can detect PA signals from a large field of view (FOV) simultaneously and thus can visualize biological dynamics at high temporal resolution in deep tissue[11–14]. However, the multi-channel detection and digitization system in PACT is complex and expensive[15–20]. In addition, PACT systems are often bulky and not suitable for portable or wearable applications[21–25]. In contrast, PAM uses point-by-point scanning of a single-element ultrasonic transducer to cover a large FOV, which limits the imaging speed and throughput[26–28]. Thus, we encounter a trade-off between the system cost and imaging throughput, which demands a new imaging method.

To address the problem, we have recently developed photoacoustic topography through an ergodic relay (PATER), which requires only a single-element transducer to capture snapshot wide-field images[10]. Topography refers to projection imaging of features along the depth direction. The acoustic ergodic relay (ER) is a waveguide that permits an acoustic wave originating from any point to reach any other point with distinct reverberant characteristics[10,29,30]. The ER can be an effective encoder to convert a 1D depth image (A-line) into a unique temporal sequence. Because of the uniqueness of each temporal signal, PA waves from the entire imaging volume

[1]Caltech Optical Imaging Laboratory, Andrew and Peggy Cherng Department of Medical Engineering, Department of Electrical Engineering, California Institute of Technology, Pasadena, CA, USA. [2]These authors contributed equally: Lei Li, Yang Li. ✉e-mail: lvw@caltech.edu

through the ER can be detected in parallel. Then, we can decode them mathematically to reconstruct 2D projection images.

Overview of the procedure

This protocol provides a comprehensive guideline for constructing the PATER system and applying it for in vivo experiments. We first introduce the PATER system, including the overview of the system, key components, image acquisition and image reconstruction. We also describe the step-by-step procedures to build and align the PATER system (see Equipment setup). PATER has two image acquisition modes: the calibration mode and the wide-field mode. During the example in vivo experiment described in the procedure, we first describe how to perform calibration imaging of the animal (Steps 1–17) to obtain the system impulse responses. Then, the wide-field measurements (Steps 18–27) capture the biological dynamics of the animal. Troubleshooting guidance for the in vivo measurements are also provided.

Advantages, limitations and applications of PATER

PATER can detect PA signals from a large imaging volume in parallel with a single-element detector, enabling snapshot wide-field imaging. We have demonstrated that PATER can provide wide-field imaging at a frame rate of 2 kHz. As an example, we have applied PATER to image cerebral hemodynamic responses, visualize blood pulse wave propagation and monitor circulating tumor cells and enable super-resolution imaging in vivo[10]. Combining with multifocal illumination, PATER improves the spatial resolution from 220 to 13 μm and provides 400 times faster imaging than conventional PAM[31]. Moreover, PATER uses only a single-element ultrasonic transducer for parallel detection of wide-field signals, which greatly simplifies the system, minimizes the size and lowers the cost. The demonstration of high-speed matching of vascular patterns shows its potential for biometric authentication on portable and wearable devices[32].

One of the limitations of our approach is that PATER can currently only image biological dynamics from areas that have high optical absorption during calibration; however, it may not be able to accurately detect features that appear in new areas that have not been subjected to calibration. This means that the system has to be re-calibrated for each new region of interest. PATER uses focused light for calibration, which restrains the imaging depths within the ~1-mm optical diffusion limit inside biological tissue. In addition, PATER's calibration is object specific. The boundary conditions between the object and the ER should remain unchanged throughout the calibration and wide-field measurements.

Experimental design

PATER system

The PATER system (Fig. 1a) consists of four major subsystems: an optical system, a mechanical scanning system, an ultrasound detection system and a data acquisition and control system. The motorized scanner, the data acquisition system and the laser are synchronized through triggers generated by the control system.

The optical system is composed of a laser system and optics for beam shaping. The laser system produces high-repetition-rate short laser pulses for PA excitation. The current PATER system uses a 532-nm Q-switched laser and a tunable dye laser. The Q-switched laser has a pulse duration of ~5 ns and a pulse repetition rate of 2 kHz. The tuning range of the dye laser is 560–690 nm, which enables imaging of various chromophores (e.g., melanin and oxy- and deoxy-hemoglobin) in vivo. In this protocol, we mainly focus on an application using the 532-nm illumination, and thus the dye laser is omitted in Fig. 1a. The laser system should produce sufficient energy for PA excitation. Currently, we deliver ~2 mJ per pulse to the tissue surface for wide-field imaging (~1 cm^2 area of illumination; the fluence is ~2 mJ/cm^2). The laser light first passes through a half-wave plate (HWP) and a polarized beamsplitter (PBS). By rotating the HWP, users can adjust the laser energy delivered to the object. Then, the laser beam goes through an iris, which controls the incident beam diameter. A lens pair (Lens 1 and Lens 2) after the iris expands the beam. The expanded beam passes through a beam sampler, which reflects a small fraction of the energy to a photodiode (PD) for energy fluctuation correction. Then, the beam reaches an optical element rotator (OER), which holds a focusing lens and an engineered diffuser. When the focusing lens is aligned in the optical path, it focuses the laser beam to the bottom surface of the prism for calibration illumination (Fig. 1b). After switching the

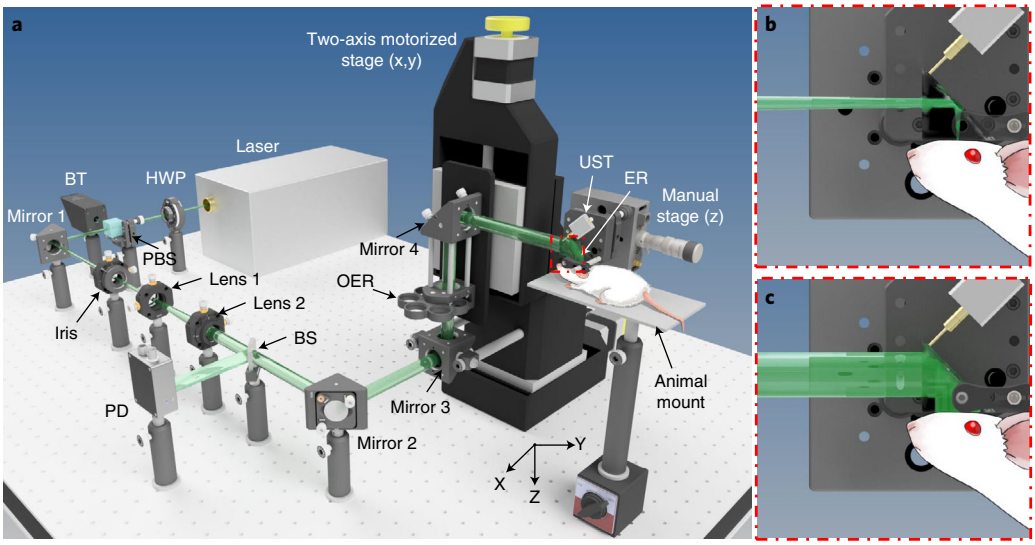

Fig. 1 | Schematic of the PATER system (drawn not to scale for clarity). a, Layout of the PATER system. BT, beam trap; BS, beam sampler; HWP, half-wave plate; OER, optical element rotator; PBS, polarized beamsplitter; PD, photodiode; UST, ultrasonic transducer. **b**, Close-up of the calibration illumination. **c**, Close-up of the wide-field illumination.

engineered diffuser into the optical path, a broad laser beam uniformly illuminates the bottom surface of the prism for wide-field illumination (Fig. 1c).

The mechanical scanning system consists primarily of a two-axis (x and y axes) motorized translational stage and a manual (z axis) stage (Fig. 1a). The motorized stage can be program-controlled to translate Mirror 3, OER and Mirror 4 to achieve 2D (x and y axes) scanning of the optical focus over the imaging surface of the ER. Currently, PATER uses an unfocused pin transducer (XMS-310, Olympus Corporation; or VP-0.5-20MHz, CTS Electronics) for ultrasound detection. In this protocol, we use XMS-310 (10-MHz central frequency, 100% one-way bandwidth and 2-mm element size) for our experimental procedures. Two low-noise amplifiers are cascaded to amplify the detected PA amplitude by 48 dB. A dual-channel high-sampling-rate digitizer is used for data acquisition. The digitizer has a maximum sampling rate of 500 million samples (MS)/s and a dynamic range of 12 bits. One input channel of the digitizer is connected to the second stage amplifier to digitize the detected PA signals. The other input channel connects to a PD to measure the laser pulse energy fluctuation for compensation.

Acoustic ER

The acoustic ER is the crucial enabling element for PATER. A perfect ER necessitates high acoustic reflectivity at the interfaces, low acoustic attenuation inside and strict geometric asymmetry about the contact point of the detector[10]. In addition, chaotic boundaries are required to guarantee ergodicity[33]. Optical transparency is also needed for optical illumination. A UV fused silica–based right-angle prism with chaotic boundaries, satisfying both the optical and acoustic requirements, can serve as the acoustic ER. It has an acoustic reflectivity of 99.99% by amplitude at the prism and air interface. In addition, the acoustic attenuation is negligible inside over the detectable pathlength range[34]. We use a low-speed diamond saw to grind all nine edges of the prism following a sawtooth pattern to obtain chaotic boundaries (Fig. 2a,b), which guarantees the ergodicity and permits the diffraction-limited spatial resolution of PATER (Fig. 2c). Three clear apertures of the prism are used for optical transmission and acoustic detection (Fig. 1b,c). One of the two leg apertures is the optical incident aperture; the other is the imaging surface and the acoustic incident aperture, which is in contact with the objects. The hypotenuse aperture is the acoustic detection surface, where the ultrasonic transducer is placed. It also reflects the incident light to the imaging surface for illumination.

Ultrasonic transducer

Given that the ER is chaotic, PATER can provide acoustic diffraction-limited resolution for wide-field imaging[33]. The spatial resolution of the PATER image is determined by the frequency bandwidth of the transducer. The wider the bandwidth, the higher the resolution. Users should choose the transducer according to the features to be imaged. An unfocused pin ultrasonic transducer is selected

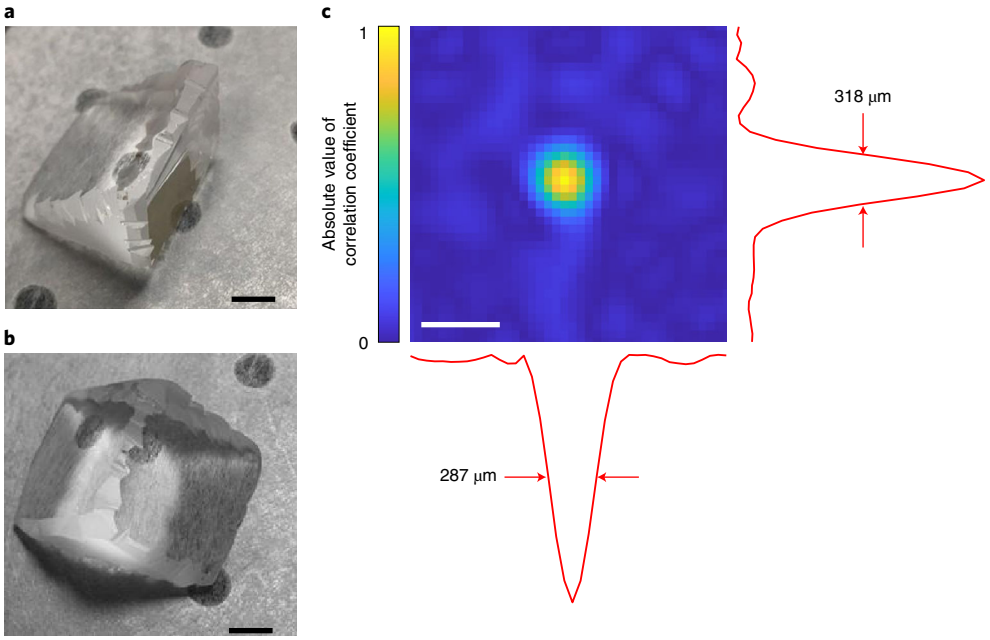

Fig. 2 | The ER and the spatial resolution of PATER. a and **b**, Photos of the ER, which is based on a UV fused silica right-angle prism. The edges are ground to ensure the ergodicity of the prism. Scale bars, 5 mm. **c**, Cross-correlation map generated from the correlation coefficients between the calibration signal of the center pixel and the signals of all the pixels in the FOV, showing the spatial resolution of PATER. Scale bar, 500 μm.

for acoustic detection. The smaller the sensing element, the wider the acoustic receiving angle, and thus the more effective at picking up the PA signals from the ER. The transducer should be placed at a corner of the detection surface of the ER to avoid geometric symmetry. To facilitate acoustic transmission, we apply ultrasound gel between the ER and the object and add a layer of high acoustic-impedance ultrasonic couplant between the ER and the transducer.

Image acquisition

In the calibration mode, focused laser illumination is used for raster scanning (Fig. 1b). Because the laser pulse width (~5 ns) is orders of magnitude narrower than the central period of the ultrasonic detector (~100 ns), and the focused beam diameter (~10 μm) is orders of magnitude smaller than the central acoustic wavelength (~600 μm), we can approximate the PA wave excited by each laser pulse as a spatiotemporal delta function. Therefore, we can quantify the system impulse response at each pixel by raster scanning the laser focus over the FOV. In the wide-field mode, the beam passing through an engineered diffuser uniformly illuminates the object (Fig. 1c). The PA signals from all pixels of the entire imaging volume are recorded in parallel, enabling snapshot wide-field imaging. We can solve an inverse problem to reconstruct wide-field images (see Image reconstruction), which map the optical absorption changes of the object.

Motor-controlling and data acquisition parameters

In the calibration mode, the motor-controlling parameters include the starting point, scanning step sizes and scanning ranges. The scanning ranges should cover the desired FOV. In general, the scanning step size should be less than or equal to half of the resolution of wide-field imaging. Using a finer step size improves the calibration image quality but prolongs scanning time. The data acquisition parameters include the trigger delay, sampling rate, data length, averaging time and data acquisition mode. The trigger delay is ~2 μs, enabling acquisition slightly before the first PA wave arrives at the ultrasonic transducer. The sampling rate is typically ~3–4 times the upper cutoff frequency of the transducer, satisfying the Nyquist sampling requirement. For example, we used a 50-MS/s sampling rate and a 100-MS/s sampling rate for transducers with upper cutoff frequencies of 15 and 25 MHz, respectively. We set the data length to 164 μs (acoustic transition time). The higher the signal-to-noise ratio (SNR) of the calibration signal, the better the reconstructed wide-field images. To improve the SNR of the calibration signal, we typically repeat the acquisition 100 times at each scanning position and use the average signal as the calibrated impulse response. To minimize the

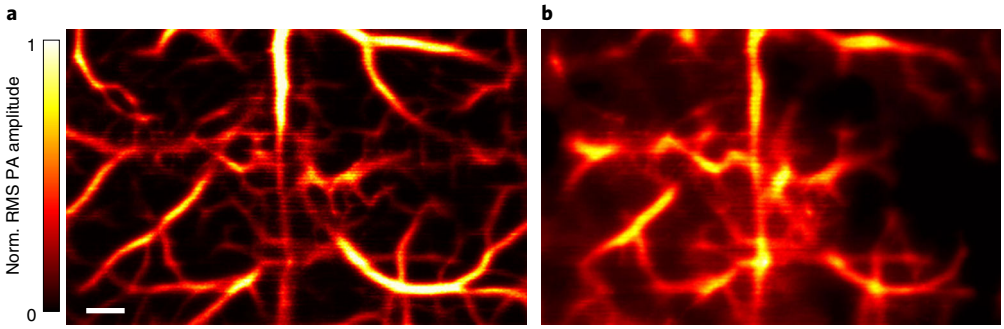

Fig. 3 | PATER of the mouse cortical vasculature in vivo. a, Calibration image of mouse brain vasculature. Scale bar, 500 μm. **b**, Reconstructed wide-field image of the calibrated area. All animal procedures were approved by the Institutional Animal Care and Use Committee of California Institute of Technology. Norm., normalized; RMS, root mean square.

motor backlash, we choose unidirectional data acquisition; that is, we acquire data only when the motor is moving forward and stop the acquisition while the motor returns. In the wide-field mode, motor scanning is disabled. The data acquisition parameters are the same as those in the calibration mode. Data averaging is optional, and the imaging frame rate can go up to 2 kHz.

Image reconstruction

A wide-field PA signal is a linear combination of the calibrated responses from all pixels:

$$s(t) = \sum_{i=1}^{N_p} k_i(t) P_i, \tag{1}$$

where s is the wide-field PA signal, t is time, i is the pixel index, N_p is the total number of pixels, P_i is the root mean square (RMS) PA amplitude and k_i is the normalized impulse response from the calibration. k_i is computed for each time point t_j via $k_i(t_j) = K_i(t_j)/\mathrm{RMS}_i$, where $K_i(t)$ is the raw calibration signal. The RMS value of $K_i(t)$ for the i^{th} pixel can be calculated as

$$\mathrm{RMS}_i = \sqrt{\frac{1}{N_t}\sum_{j=1}^{N_t}\left[K_i(t_j)\right]^2}, \tag{2}$$

where N_t is the number of sampled time points, and t is time. A calibration image is a 2D density plot of RMS_i over all pixels.

After data acquisition, all the signals are digitized, and we can recast Eq. (1) to matrix form:

$$\boldsymbol{s} = \boldsymbol{K}\boldsymbol{P}, \tag{3}$$

where $\boldsymbol{K} = \left[k_1, k_2, \ldots, k_{N_p}\right]$ is the system matrix. We can reconstruct the wide-field image $\boldsymbol{P}$ from the signal $\boldsymbol{s}$ by solving Eq. (3), where a two-step iterative shrinkage/thresholding (TwIST) algorithm[35] is used. We solve Eq. (3) for $\boldsymbol{P}$ as a minimizer of the objective function:

$$\hat{\boldsymbol{P}} = \arg\min_{\boldsymbol{P}} ||\boldsymbol{s} - \boldsymbol{K}\boldsymbol{P}||^2 + 2\lambda\Phi_{\mathrm{TV}}(\boldsymbol{P}), \tag{4}$$

where $\Phi_{\mathrm{TV}}(\boldsymbol{P})$ is the total variation of $\boldsymbol{P}$, and λ is the regularization parameter. To minimize computational instability and ensure reconstruction image quality, pixels with RMS values lower than twice (6 dB) the noise amplitude are excluded from the system matrix $\boldsymbol{K}$. Examples of the calibration and wide-field images of the mouse cortical vasculature are shown in Fig. 3; the raw data can be accessed by using the link provided in the Data availability statement. The reconstruction program is provided as an example (Supplementary Software 1); however, the regularization parameter may need to be readjusted depending on the application.

Materials

Biological materials

- *Mice*. For brain imaging experiments, we use 6- to 12-week-old (no specific sex requirement) Swiss Webster mice (Hsd: ND4, 20–30 g; Envigo, cat. no. 032) or wild-type C57BL/6J mice (The Jackson Laboratory, cat. no. 000664). For imaging ears or other body sites, we typically use 8- to 12-week-old

nude mice (Hsd: Athymic Nude-FoxlNU, 20−30 g; Envigo, cat. no. 069) **! CAUTION** All experiments using animals must be carried out in conformity with the applicable national guidelines and regulations. The animal procedures described within this protocol were approved by the Institutional Animal Care and Use Committee of California Institute of Technology (IA20-1737).

Reagents

- Deionized water
- Ultrasound gel (MFIMedical, cat. no. PKR-03-02) to facilitate acoustic coupling between objects and the ER
- High acoustic-impedance ultrasonic couplant (Berg Engineering & Sales, cat. no. ECHO-Z-PLUS-F-04) to facilitate acoustic coupling between the ER and the ultrasonic transducer
- Isoflurane (Zoetis, cat. no. 10015516)
- Alcohol swabs (VWR, cat. no. BD326895)
- Hair-removing lotion (Nair; CVS, cat. no. 339826)
- Ophthalmic ointment (Pharmaderm, cat. no. NDC 17033-211-38)

Equipment

- Pulsed pump laser (INNOSAB IS8II-E, Edgewave GmbH, 532 nm, 5-ns pulse width, 2-kHz pulse repetition rate) **! CAUTION** The laser is a class IV laser. Wear laser protection goggles during operation.
- Laser line mirror (NB1-K12, Thorlabs)
- HWP (WPH10M-532, Thorlabs)
- PBS (10FC16PB.3, Newport) in combination with the HWP to adjust laser energy
- Beam trap (BT610, Thorlabs)
- Beam-expanding lens pair (LC1715-A (f = −50.0 mm) and LA1433-A (f = 150.0 mm), Thorlabs)
- BS (BSF10-A, Thorlabs)
- PD (APD430A2, Thorlabs)
- Focusing lens (LA1509 (f = 100.0 mm), Thorlabs)
- Engineered diffuser (EDC-5-A-1r, RPC Photonics) to homogenize the laser light for wide-field illumination
- Right-angle prism (PS615, Thorlabs)
- Digital low-speed diamond saw (SYJ-150, MTI Co.)
- Beam profiler (SP620U, Ophir)
- Motorized linear translation stage (PLS-85, PI GmbH)
- Motor driver (CW215, Circuit Specialists)
- Manual linear translation stage (NFL5D, Thorlabs)
- Ultrasonic transducer (XMS-310, Olympus; or VP-0.5-20MHz, CTS Electronics)
- Wideband signal amplifier (ZFL-500LN+, Mini-Circuits)
- Computer
- Dual-channel digitizer (ATS9350, Alazar Technologies)
- Multifunction input/output (I/O) device (PCIe-6321, National Instruments) to control the laser, the scanner and the data acquisition system
- Custom-made animal holder (Supplementary Data 1); commercial alternative: mouse stereotaxic instrument (Items 53800 and 51730, Stoelting)
- Hair trimmer (Model 9854-600, Wahl Clipper)
- Thermocouple (SA1-E, Omega Engineering)
- Heater (SRFG-303/10, Omega Engineering)
- Temperature controller (Dwyer 32B-33, Cole-Parmer Instruments) in combination with the thermocouple and the heater to regulate the animal's temperature
- Breathing anesthesia system (E-Z Anesthesia, E-Z Systems)
- Polyethylene membrane (Cling Wrap, Glad)
- Double-sided tape (Scotch tape, 3M)
- Paper tape (3M)
- Silicone tubing (HelixMark, VWR International)
- Scientific software (LabVIEW, National Instruments, https://www.ni.com/en-us/shop/labview.html; MATLAB, MathWorks, https://www.mathworks.com/products/matlab.html) for developing the data acquisition program and image reconstruction algorithm
- MATLAB reconstruction program (Supplementary Software 1)

Equipment setup

Setup and alignment of the PATER system

The experimental setup shown in Fig. 1 is required for performing PATER imaging. In addition to the setup, good alignment is essential for high-quality PATER imaging. The procedure below should be followed to build and align the PATER system:

1 Have the vendor set up the optical table, as shown in Fig. 1a.

2 Set up a computer with both the dual-channel digitizer and the multifunction I/O device installed.

3 Have the vendor install the laser, as shown in Fig. 1a. **! CAUTION** The laser is a class IV laser. Wear laser protection goggles during operation.

4 Set up the HWP and the PBS to adjust the laser power. ▲ **CRITICAL** The beam trap should be installed to absorb the laser beam reflected by the PBS.

5 Install the iris to control the laser beam diameter. Mirror 1 in Fig. 1a is used to turn the beam direction; it is not an essential part of the system.

6 After the iris, set up the lens pair (Lens 1 and Lens 2 in Fig. 1a) to expand the laser beam. ▲ **CRITICAL** The laser beam should coincide with the optical axes of Lens 1 and Lens 2.

7 Install the beam sampler and the PD to sample the laser beam for energy fluctuation correction. Connect the output of the PD to one of the input channels of the dual-channel digitizer.

8 Following Fig. 1a, install Mirrors 2–4, the two-axis (x and y axes) motorized translational stage and the manual (z axis) stage. ▲ **CRITICAL** Mirrors 2–4 should be adjusted such that the incident and reflected laser beams are perpendicular to each other.

9 Set up the OER between Mirror 3 and Mirror 4. Install the focusing lens and the engineered diffuser on the OER. ▲ **CRITICAL** When switched into the optical path, the optical axes of the focusing lens and the engineered diffuser should coincide with the laser beam.

10 Use a low-speed diamond saw to grind all nine edges of a UV fused silica–based right-angle prism to obtain the acoustic ER (Fig. 2a,b). Whereas chaotic boundaries and ergodicity can be obtained in various patterns, we choose to grind the prism edges following a sawtooth pattern, which has been experimentally proven effective (Fig. 2c). There is no requirement on the flatness of the ground surfaces.

11 Install the ER on the z-axis stage (Fig. 1a).

12 Place the ultrasonic transducer at a corner of the detection surface of the ER (the hypotenuse surface of the prism in Fig. 1b). ▲ **CRITICAL** Make sure that the transducer is in good contact with the ER and that the axis of the transducer is perpendicular to the ER detection surface.

13 Connect the output of the transducer to the input of the cascaded amplifiers, and connect the output of the cascaded amplifiers to the other input channel of the dual-channel digitizer.

14 Set up the animal holder for animal imaging in vivo. The 3D models of the animal holder components can be found in Supplementary Data 1.

15 Start the calibration mode by rotating the OER to switch the focusing lens into the optical path (Fig. 1b). ▲ **CRITICAL** In the calibration mode, a tight optical focus is scanned over the object to measure the impulse response of each pixel.

16 Use a beam profiler to check the optical alignment on the imaging surface of the ER (the bottom surface of the prism in Fig. 1b). Adjust the distance between the beam profiler and the ER to overlap the imaging surface of the ER and the focal plane of the beam profiler.

17 Manually adjust the z-axis stage (Fig. 1a) to locate a position where the laser beam has the smallest diameter, indicating that the laser beam is focused on the imaging surface of the ER.

18 Move the x-axis stage across the whole scanning range and check if the laser beam is in focus for the whole range. If not, adjust Mirrors 2 and 3 (Fig. 1a) to ensure normal incidence of the laser beam into the focusing lens.

19 Move the y-axis stage across the whole scanning range and check if the laser beam is in focus for the whole range. If not, adjust Mirrors 3 and 4 (Fig. 1a) to ensure normal incidence of the laser beam into the ER.

20 Repeat Steps 18 and 19 until the laser beam is in focus for the entire imaging surface. Figure 2c shows the experimentally measured resolution of the PATER system after it is well aligned.

21 When imaging animals in vivo, move the z-axis stage to transfer the laser focus into the tissue (~300–400 μm in depth) to make sure that the focal zone of the calibration light covers the ROI along the depth direction.

22 Start the wide-field mode by rotating the OER to switch the engineered diffuser into the optical path (Fig. 1c). Check if the broad laser beam covers the FOV. If not, adjust the linear translation stages to ensure that the light uniformly illuminates the entire FOV. ▲ **CRITICAL** Users should also note that the wide-field illumination beam is within or equal to the calibrated area.

Procedure

▲ **CRITICAL** To illustrate our approach, we here describe the procedures for in vivo imaging of the mouse cortical vasculature (ND4, Swiss Webster, body weight: 20–30 g). The procedure will need to be modified accordingly for other imaging applications.

1 Warm up the laser 30 min before the experiment.

2 Set the temperature controller to 38 °C and turn on the heater. Wait for 5 min until the temperature reaches equilibrium. Throughout the experiment, the animal body temperature is regulated toward 38 °C.

3 Weigh the animal and then place it in an induction chamber connected to an isoflurane vaporizer. Induce anesthesia with a mixture of medical-grade air and 5% (vol/vol) vaporized isoflurane at a flow rate of 1–1.5 liters/min for ~5 min. Monitor the anesthetic depth by testing the animal's response to tail or toe pinches. A lack of response indicates that the animal is adequately anesthetized. Once fully anesthetized, transfer the mouse to the animal holder and change the isoflurane concentration to 2% (vol/vol) at a flow rate of 1–1.5 liters/min through a nosecone.
▲ **CRITICAL STEP** The operator should wear clean examination gloves, a face mask and a clean laboratory coat.

4 Trim the animal's hair in the ROI (e.g., head) as well as the surrounding area.

5 Apply hair-removing lotion to the trimmed area, wait for 1–3 min and then clean with warm water.

6 Disinfect the depilated skin by using alcohol swabs, incise the scalp along the midline and expose the skull.

7 Apply a layer of ultrasound gel (~1–2 mm thick) to the exposed skull.

8 Transfer the animal with the holder to the imaging table. Loosely fix the body and the four legs onto the holder with paper tape to restrain motions during data acquisition.

9 Place the ROI under the ER and lift the animal holder until the skull touches the imaging surface of the ER. Gently push the mouse skull against the ER to ensure tight contact between them.
▲ **CRITICAL STEP** Avoid trapping air bubbles in the middle.

10 Continuously supply a mixture of medical-grade air and 1% (vol/vol) isoflurane at a flow rate of 1–1.5 liters/min to the animal through the nosecone.
▲ **CRITICAL STEP** The flow rate varies with the body weight of the animal. Please refer to the instructions of each specific anesthesia system.

11 Apply ophthalmic ointment to the corneal surfaces to prevent dryness, and cover the eyes to prevent accidental laser damage.

12 Switch the focusing lens into the optical path, as shown in Fig. 1b, and begin with the calibration mode.

13 Start the control and data acquisition program in LabVIEW. Turn on the laser, select the low power continuous-wave mode and locate the position of the laser spot on the imaging surface.
! **CAUTION** The laser is a class IV laser. Wear laser protection goggles during operation. Move the laser spot to the desired location and set the scanning ranges and step sizes of both the x and y axes to the designated values to cover the ROI.

14 Switch the laser to the external triggering mode and start laser firing.
! **CAUTION** The laser pulse energy and the pulse repetition rate should be checked carefully according to laser safety.

15 Execute a quick raster scan with data acquisition.

16 Check the calibration image of the quick scan to ensure that the SNR is good and that the ROI fits in the FOV. If the SNR is low, adjust the laser illumination fluence and repeat. If the ROI is not entirely within the FOV, adjust the scanning ranges and repeat.
? **TROUBLESHOOTING**

17 Set the scanning and averaging parameters (typically 100–200-time averaging at every scanning position) and start the calibration scanning and data acquisition.

18 Move the laser beam to the center of the ROI after calibration scanning.

19 Rotate the OER to switch the engineered diffuser in the optical path (Fig. 1c). Set the laser to the continuous-wave mode and ensure that the broad laser beam uniformly illuminates the ROI. Note that the wide-field beam–illuminated area should be within the calibrated area.

20 Switch the laser to the external triggering mode and start laser firing for pre-acquisition.

21 Check the SNR of the pre-acquisition data. If the SNR is low, adjust the laser illumination fluence and repeat. The SNR is considered low if the r.m.s. value of the pre-acquisition data is lower than twice (6 dB) the noise amplitude.
? **TROUBLESHOOTING**

22 Set the data acquisition parameters (e.g., trigger delay, 2.2 μs; sampling rate, 100 MHz; data length, 16,384 points; averaging time, 100×) and start the wide-field image acquisition.
23 Stop laser firing after completion of the data acquisition.
24 Run the MATLAB reconstruction program (Supplementary Software 1) to reconstruct wide-field images by using both the calibration and wide-field data.
? TROUBLESHOOTING
25 Lower the animal holder and detach the animal from the ER.
26 Increase the isoflurane concentration to 5% (vol/vol) to euthanize the animal, followed by cervical dislocation to ensure death. Dispose of the carcass by following proper procedures.
27 Turn off the laser and isoflurane supply and clean the imaging table.

Troubleshooting

Step 16: no PA signal or weak PA signal

When no PA signal or only a weak PA signal can be detected, first make sure that the ultrasonic transducer is in good contact with the ER and that the axis of the transducer is perpendicular to the ER detection surface. Second, check to ensure that the high acoustic-impedance ultrasonic couplant (not ultrasound gel) is correctly applied between the transducer and the ER detection surface. Third, gentle force should be applied to contact the transducer with the ER and make sure that no air gap is trapped in the middle. Fourth, verify that the signal amplifiers are powered and that all cables are connected correctly and robustly and are functioning properly. Fifth, make sure that the object is illuminated with enough laser energy and that the laser is operated under external triggering mode and synchronized with the data acquisition system.

To locate PA signals initially, users can set the delay between laser firing and data acquisition to zero and set the data recording length to ~500 μs. After the PA signals are observed, change the trigger delay and data recording length to designated values.

Steps 16 and 21: low SNR of the calibration or wide-field signals

In case of a low SNR of the calibration or wide-field signals, refer to 'Step 16: no PA signal or weak PA signal' first to make sure that the system is detecting PA signals. If PA signals are detected but noisy, users can check the steps below. First, make sure that the optical path is well aligned. Especially for the calibration mode, make sure that the object is within the optical focal zone. Second, make sure that the system is well shielded and grounded. The motor drivers and control circuits should be shielded, and power supply cables should be grounded. Third, gradually increase the laser fluence and average more times to improve the SNR.

Step 24, low quality of reconstructed wide-field images

If the quality of the reconstructed wide-field images is low, users should first check whether the wide-field beam–illuminated area is beyond the calibrated area. Users can adjust the distance between the engineered diffuser and the object to change the size of the wide-field illumination beam. If the

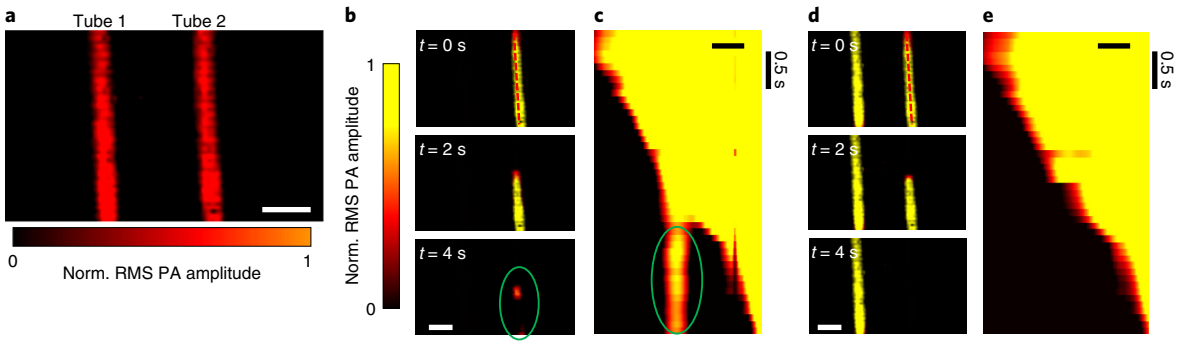

Fig. 4 | Reconstruction artifacts caused by signals from uncalibrated areas. Two tubes filled with blood were placed on the imaging surface. While Tube 1 served as the control without flow, blood flowed through Tube 2 during wide-field measurements. **a**, Calibration image of the two tubes. Scale bar, 2 mm. **b**, Reconstructed wide-field images with Tube 1 uncalibrated. Signals from both tubes were captured in wide-field imaging. The reconstruction artifacts are marked by a green ellipse. **c**, Space-time domain plot of pixels along the axis of Tube 2 in **b**, revealing the reconstruction artifacts, marked by a green ellipse. **d**, Reconstructed wide-field images with both tubes calibrated, showing no artifacts. **e**, Space-time domain plot of pixels along the axis of Tube 2 in **d**, illustrating a correct reconstruction. Scale bars in **b**–**e**, 1 mm. Images adapted from ref. [10].

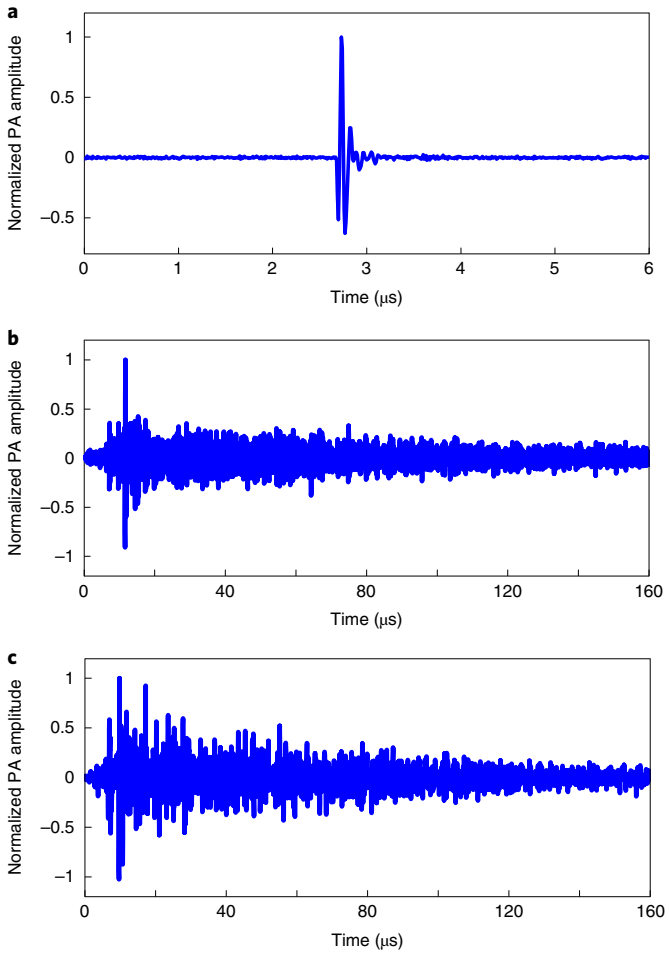

Fig. 5 | Temporal signatures of the PA signals. a and **b**, PA signals from a point source detected by a conventional PAM system (**a**) and PATER (**b**). The useful signal in **a** lasts ~500 ns. PATER records the signal in **b** for 160 μs. **c**, Wide-field signal recorded by using PATER for 160 μs.

wide-field signal mixes with signals from uncalibrated areas, it will yield incorrect reconstruction images, as demonstrated in Fig. 4. As shown in Fig. 4a, two tubes filled with blood were imaged. During the calibration step, we scanned Tube 2 only, leaving Tube 1 uncalibrated. In the wide-field mode, we illuminated both tubes to capture blood flushing out of Tube 2. The reconstructed images at different time points are shown in Fig. 4b, where reconstruction artifacts are labeled by a green ellipse. A space-time domain plot of pixels along the dashed line in Fig. 4b (top panel) also reveals the artifacts, marked by a green ellipse (Fig. 4c). When both tubes were calibrated, correct images could be reconstructed (Fig. 4d,e). Another possibility is a low SNR of the calibration images or wide-field images; please refer to 'Steps 16 and 21: low SNR of the calibration or wide-field signals'. This problem is also probably caused by boundary condition changes during the processes of calibration and wide-field imaging. Animal motion, primarily respiratory motion, should be minimized, and the contact area between the animal and the ER should remain unchanged throughout the experiment. Make sure that the animal is properly and securely fixed and that the anesthesia system functions well. Check the animal holder and inhalation gas supply and make sure that the animal is anesthetized and can breathe freely. Users should gently apply force to attach the animal against the ER to ensure tight contact.

Timing

The total time required to complete the protocol is ~12 h for setup and alignment of the PATER system and 130 min for calibration and imaging

Equipment setup, setup and alignment of the PATER system: ~12 h

Steps 1–14, system and animal preparation: ~30 min

Steps 15–16, adjustment of the scanning range to fit the ROI: ~10 min
Step 17, calibration imaging: varies on the scanning range, step size, averaging parameter and laser repetition rate (e.g., scanning of a 6 × 6 mm^2 area with a step size of 30 μm and 100-time averaging at 2-kHz laser repetition rate takes ~50 min)
Steps 18–23, wide-field imaging: depends on the number of frames needed for recording the targeted dynamics (typically, ~1–10 min)
Steps 24–27, remaining procedures: the time of image reconstruction depends on the number of reconstructed frames (typically, ~30 min for 120 frames on a workstation (Intel Xeon E5-2620v2, 2.10 GHz, 8 cores and 16 GB RAM)). Steps 25–27 typically take ~20–30 min. Users can perform Step 24 and Steps 25–27 in parallel

Anticipated results

This protocol, based on ref. [10], provides a step-by-step guideline on how to apply PATER to snapshot in vivo imaging of a mouse brain. When operated correctly, PATER can provide high-throughput topographic images of optical absorption.

In the calibration mode, a focused optical beam is used for scanning. The detected PA waves through the ER are different from A-line signals in a conventional PAM, which represents a 1D depth-resolved image (Fig. 5a). However, the PA signal with randomized temporal signatures, encoded by the ER, is much longer (Fig. 5b). After raster scanning the optical focus over the object, PATER yields a 2D projection image of the 3D object. Example images can be found in Fig. 3 of this protocol and in Figs. 3–5 of ref. [10].

In the wide-field mode, a broad beam illuminates the object uniformly. The detected PA signals are a weighted summation of the calibration signals (Fig. 5c). In this mode, PA signals from the entire FOV can be received in parallel. We can mathematically compute the 2D projection images, which represent the optical absorption changes of the object. As shown in Fig. 6, PATER captures the processes of blood flushing in and out of an S-shaped tube.

More wide-field imaging results are shown in Fig. 7 and can be found in ref. [10]. Taking advantage of the high-speed snapshot wide-field imaging, PATER can be used to visualize the blood pulse wave propagation at multiple sites simultaneously in mice in vivo (Fig. 7a–g and Fig. 4 of ref. [10]) and tracks circulating melanoma tumor cells in the brain and localizes them at super-resolution in vivo (Fig. 7h–k and Fig. 5 from ref. [10]).

PATER requires that the boundary conditions between the object and ER remain unchanged throughout the experiment. A successful wide-field reconstruction relies on the assumption that the

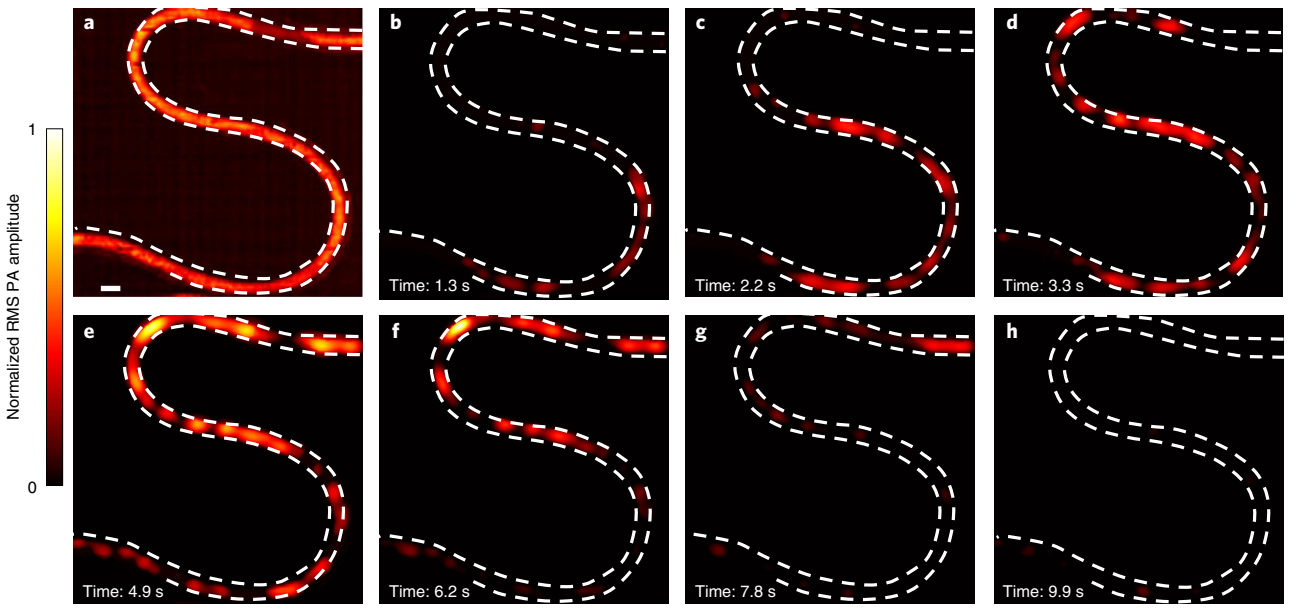

Fig. 6 | Blood flushing in and out of a tube. a, RMS image of an S-shaped tube filled with blood. Scale bar, 1 mm. **b**–**h**, Wide-field images showing blood flushing in and out of the tube.

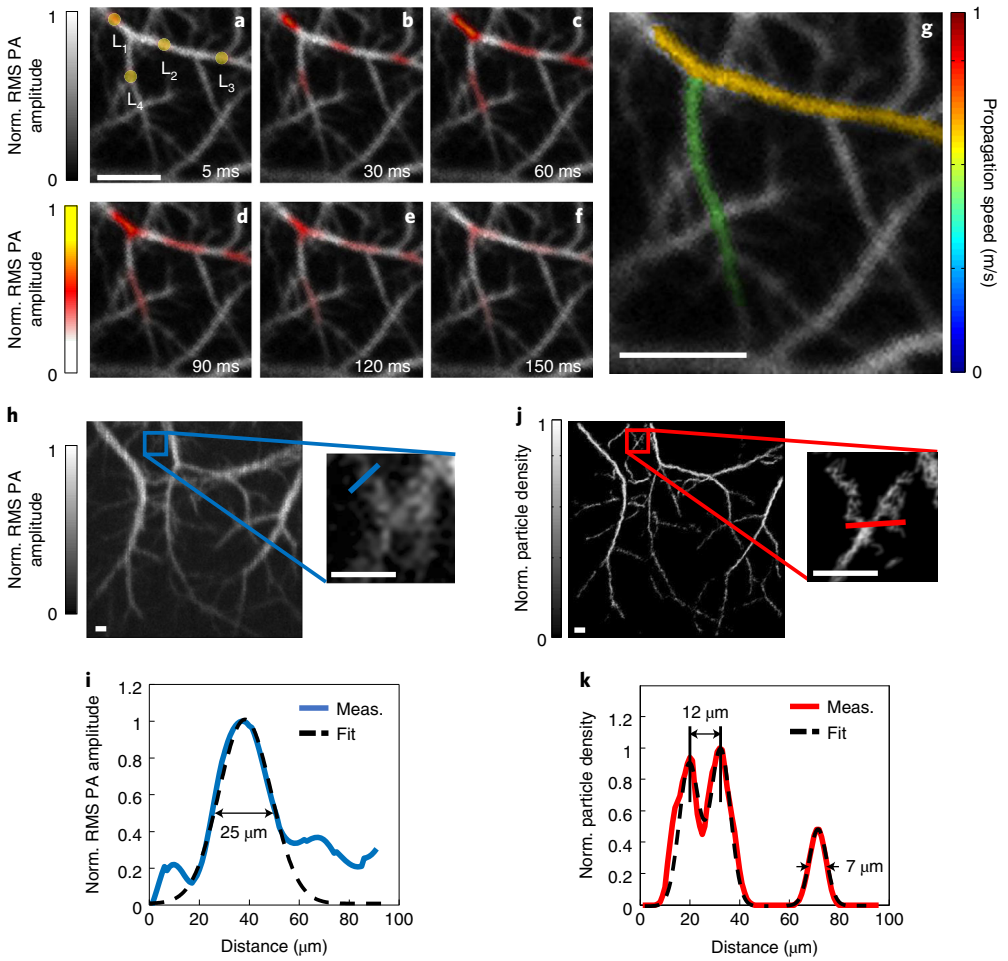

Fig. 7 | PATER of biological dynamics in vivo. a–f, Wide-field images showing thermal wave propagation in the mouse middle cerebral arteries. The yellow circles in **a**, labeled 'L_1–L_4', indicate locations of the laser heating spots during recording. The overlay images show the thermal wave signals in color and the background blood signals in gray. **g**, Map of pulse wave velocity at two branches of the middle cerebral arteries. **h**, Calibration image of the mouse brain and a zoomed-in view of the blue boxed region showing a group of small vessels. Scale bars in **a** and **g**, 500 μm. **i**, Plot of the profile along the blue line in the zoomed-in view in **h** and a Gaussian fit. **j**, Localization map of circulating tumor cells and a zoomed-in view of the red boxed region showing the same region as the blue boxed region in **h**. Scale bars in **h** and **j**, 100 μm. **k**, Plot of the profile along the red line in the zoomed-in view in **j** and a three-term Gaussian fit. The two neighboring vessels branching out from each other can be separated at a distance of 12 μm, and the full width at half maximum for the small vessel is 7 μm. Images adapted from ref. [10]. All animal procedures were approved by the Institutional Animal Care and Use Committee of California Institute of Technology. Meas., measurement.

wide-field measurement is a consistent linear combination of the calibrated system impulse responses. Once the boundary conditions change because of movements of the object or the instability of the system, the calibrated impulse responses will be different from the system responses during the wide-field measurements, resulting in reconstruction artifacts and incorrect measurements. Those issues can be solved, however, by a universal calibration method, which is beyond the scope of this protocol.

Reporting Summary

Further information on research design is available in the Nature Research Reporting Summary linked to this article.

Data availability

All data generated or analyzed within this study are included in the article and ref. [10]. The raw data for Figs. 2 and 3 can be downloaded via the following links: Fig. 2, https://figshare.com/articles/

dataset/Data_for_Fig_2/12950798; Fig. 3, https://figshare.com/articles/dataset/Data_for_Fig_3/12591953. All other raw data are available from the corresponding author upon request.

Code availability

The reconstruction algorithm and data processing methods are described in detail in this protocol. The reconstruction algorithm is provided with this protocol as Supplementary Software 1.

References

1. Weber, J., Beard, P. C. & Bohndiek, S. E. Contrast agents for molecular photoacoustic imaging. *Nat. Methods* **13**, 639–650 (2016).
2. Ntziachristos, V. Going deeper than microscopy: the optical imaging frontier in biology. *Nat. Methods* **7**, 603–614 (2010).
3. Wang, L. H. V. & Hu, S. Photoacoustic tomography: in vivo imaging from organelles to organs. *Science* **335**, 1458–1462 (2012).
4. Zhang, H. F., Maslov, K. & Wang, L. V. In vivo imaging of subcutaneous structures using functional photoacoustic microscopy. *Nat. Protoc.* **2**, 797–804 (2007).
5. Beard, P. C. Biomedical photoacoustic imaging. *Interface Focus* **1**, 602–631 (2011).
6. Xu, M. & Wang, L. V. Universal back-projection algorithm for photoacoustic computed tomography. *Phys. Rev. E Stat. Nonlin. Soft Matter Phys.* **71**, 016706 (2005).
7. Matthews, T. P., Poudel, J., Li, L., Wang, L. V. & Anastasio, M. A. Parameterized joint reconstruction of the initial pressure and sound speed distributions for photoacoustic computed tomography. *SIAM J. Imaging Sci.* **11**, 1560–1588 (2018).
8. Li, L. et al. Single-impulse panoramic photoacoustic computed tomography of small-animal whole-body dynamics at high spatiotemporal resolution. *Nat. Biomed. Eng.* **1**, 0071 (2017).
9. Wang, L. V. & Yao, J. A practical guide to photoacoustic tomography in the life sciences. *Nat. Methods* **13**, 627–638 (2016).
10. Li, Y. et al. Snapshot photoacoustic topography through an ergodic relay for high-throughput imaging of optical absorption. *Nat. Photonics* **14**, 164–170 (2020).
11. Li, L. et al. Small near-infrared photochromic protein for photoacoustic multi-contrast imaging and detection of protein interactions in vivo. *Nat. Commun.* **9**, 2734 (2018).
12. Zhang, P. et al. High-resolution deep functional imaging of the whole mouse brain by photoacoustic computed tomography in vivo. *J. Biophotonics* **11**, e201700024 (2018).
13. Zhang, P., Li, L., Lin, L., Shi, J. & Wang, L. V. In vivo superresolution photoacoustic computed tomography by localization of single dyed droplets. *Light Sci. Appl.* **8**, 36 (2019).
14. Jathoul, A. P. et al. Deep in vivo photoacoustic imaging of mammalian tissues using a tyrosinase-based genetic reporter. *Nat. Photonics* **9**, 239–246 (2015).
15. Yao, J. et al. Multiscale photoacoustic tomography using reversibly switchable bacterial phytochrome as a near-infrared photochromic probe. *Nat. Methods* **13**, 67–73 (2016).
16. Wu, Z. et al. A microrobotic system guided by photoacoustic computed tomography for targeted navigation in intestines *in vivo*. *Sci. Robot.* **4**, eaax0613 (2019).
17. Li, L. et al. Label-free photoacoustic tomography of whole mouse brain structures *ex vivo*. *Neurophotonics* **3**, 035001 (2016).
18. Yeh, C. et al. Dry coupling for whole-body small-animal photoacoustic computed tomography. *J. Biomed. Opt.* **22**, 41017 (2017).
19. Razansky, D. et al. Multispectral opto-acoustic tomography of deep-seated fluorescent proteins in vivo. *Nat. Photonics* **3**, 412–417 (2009).
20. Imai, T. et al. High-throughput ultraviolet photoacoustic microscopy with multifocal excitation. *J. Biomed. Opt.* **23**, 1–6 (2018).
21. Qu, Y. et al. Dichroism-sensitive photoacoustic computed tomography. *Optica* **5**, 495–501 (2018).
22. Razansky, D., Buehler, A. & Ntziachristos, V. Volumetric real-time multispectral optoacoustic tomography of biomarkers. *Nat. Protoc.* **6**, 1121–1129 (2011).
23. Li, L., Zhu, L., Shen, Y. & Wang, L. V. Multiview Hilbert transformation in full-ring transducer array-based photoacoustic computed tomography. *J. Biomed. Opt.* **22**, 76017 (2017).
24. Laufer, J. et al. In vivo preclinical photoacoustic imaging of tumor vasculature development and therapy. *J. Biomed. Opt.* **17**, 056016 (2012).
25. Ellwood, R., Ogunlade, O., Zhang, E., Beard, P. & Cox, B. Photoacoustic tomography using orthogonal Fabry–Pérot sensors. *J. Biomed. Opt.* **22**, 41009 (2016).
26. Li, L. et al. Fully motorized optical-resolution photoacoustic microscopy. *Opt. Lett.* **39**, 2117–2120 (2014).
27. Yao, J. et al. High-speed label-free functional photoacoustic microscopy of mouse brain in action. *Nat. Methods* **12**, 407–410 (2015).
28. Hsu, H.-C. et al. Dual-axis illumination for virtually augmenting the detection view of optical-resolution photoacoustic microscopy. *J. Biomed. Opt.* **23**, 1–7 (2018).
29. Draeger, C. & Fink, M. One-channel time reversal of elastic waves in a chaotic 2D-silicon cavity. *Phys. Rev. Lett.* **79**, 407 (1997).

30. Ing, R. K., Quieffin, N., Catheline, S. & Fink, M. In solid localization of finger impacts using acoustic time-reversal process. *Appl. Phys. Lett.* **87**, 204104 (2005).
31. Li, Y., Wong, T. T., Shi, J., Hsu, H.-C. & Wang, L. V. Multifocal photoacoustic microscopy using a single-element ultrasonic transducer through an ergodic relay. *Light Sci. Appl.* **9**, 1–7 (2020).
32. Li, Y. et al. Photoacoustic topography through an ergodic relay for functional imaging and biometric application in vivo. *J. Biomed. Opt.* **25**, 1–8 (2020).
33. Fink, M. & de Rosny, J. Time-reversed acoustics in random media and in chaotic cavities. *Nonlinearity* **15**, R1 (2001).
34. Eder, F. X. *Moderne Messmethoden der Physik. Bd 1*. 2., erweiterte Aufl. Edn (Deutscher Verlag der Wissenschaften, 1960).
35. Bioucas-Dias, J. M. & Figueiredo, M. A. T. A new TwIST: two-step iterative shrinkage/thresholding algorithms for image restoration. *IEEE Trans. Image Process.* **16**, 2992–3004 (2007).

Acknowledgements

This work was supported in part by National Institutes of Health grants R01 CA186567 (NIH Director's Transformative Research Award), R01 NS102213, U01 NS099717 (BRAIN Initiative), R35 CA220436 (Outstanding Investigator Award) and R01 EB028277.

Author contributions

L.L. and Y.L. developed the imaging system. L.L., Y.L. and Y.Z. designed and performed the experiments. L.V.W. supervised the study. All authors contributed to writing the manuscript.

Competing interests

L.V.W. has financial interests in Microphotoacoustics, Inc.; CalPACT, LLC; and Union Photoacoustic Technologies, Ltd., which did not support this work.

Additional information

Supplementary information The online version contains supplementary material available at https://doi.org/10.1038/s41596-020-00487-w.

Correspondence and requests for materials should be addressed to L.V.W.

Peer review information *Nature Protocols* thanks Miya Ishihara, Guenther Paltauf and the other, anonymous, reviewer(s) for their contribution to the peer review of this work.

Reprints and permissions information is available at www.nature.com/reprints.

Publisher's note Springer Nature remains neutral with regard to jurisdictional claims in published maps and institutional affiliations.

Received: 17 July 2020; Accepted: 16 December 2020;
Published online: 12 April 2021

Related links
Key references using this protocol
Li, Y. et al. *Nat. Photonics* **14**, 164–170 (2020): https://doi.org/10.1038/s41566-019-0576-2
Li, Y. et al. *J. Biomed. Opt.* **25**, 070501 (2020): https://doi.org/10.1117/1.JBO.25.7.070501
Li, Y. et al. *Light Sci. Appl.* **9**, 135 (2020): https://doi.org/10.1038/s41377-020-00372-x

nature research

Corresponding author(s): Lihong V. Wang

Last updated by author(s): Nov 16, 2020

Reporting Summary

Nature Research wishes to improve the reproducibility of the work that we publish. This form provides structure for consistency and transparency in reporting. For further information on Nature Research policies, see Authors & Referees and the Editorial Policy Checklist.

Statistics

For all statistical analyses, confirm that the following items are present in the figure legend, table legend, main text, or Methods section.

n/a	Confirmed
☒	☐ The exact sample size (*n*) for each experimental group/condition, given as a discrete number and unit of measurement
☒	☐ A statement on whether measurements were taken from distinct samples or whether the same sample was measured repeatedly
☒	☐ The statistical test(s) used AND whether they are one- or two-sided *Only common tests should be described solely by name; describe more complex techniques in the Methods section.*
☒	☐ A description of all covariates tested
☒	☐ A description of any assumptions or corrections, such as tests of normality and adjustment for multiple comparisons
☒	☐ A full description of the statistical parameters including central tendency (e.g. means) or other basic estimates (e.g. regression coefficient) AND variation (e.g. standard deviation) or associated estimates of uncertainty (e.g. confidence intervals)
☒	☐ For null hypothesis testing, the test statistic (e.g. *F*, *t*, *r*) with confidence intervals, effect sizes, degrees of freedom and *P* value noted *Give P values as exact values whenever suitable.*
☒	☐ For Bayesian analysis, information on the choice of priors and Markov chain Monte Carlo settings
☒	☐ For hierarchical and complex designs, identification of the appropriate level for tests and full reporting of outcomes
☒	☐ Estimates of effect sizes (e.g. Cohen's *d*, Pearson's *r*), indicating how they were calculated

Our web collection on statistics for biologists contains articles on many of the points above.

Software and code

Policy information about availability of computer code

Data collection	LabVIEW 2015, AlazarTech ATS-VI 5.8.3
Data analysis	Matlab 2019a

For manuscripts utilizing custom algorithms or software that are central to the research but not yet described in published literature, software must be made available to editors/reviewers. We strongly encourage code deposition in a community repository (e.g. GitHub). See the Nature Research guidelines for submitting code & software for further information.

Data

Policy information about availability of data

All manuscripts must include a data availability statement. This statement should provide the following information, where applicable:

- Accession codes, unique identifiers, or web links for publicly available datasets
- A list of figures that have associated raw data
- A description of any restrictions on data availability

All data generated or analyzed within this study are included in the paper and its Supplementary Information and are available from the corresponding author upon request.

Field-specific reporting

Please select the one below that is the best fit for your research. If you are not sure, read the appropriate sections before making your selection.

☒ Life sciences ☐ Behavioural & social sciences ☐ Ecological, evolutionary & environmental sciences

Life sciences study design

All studies must disclose on these points even when the disclosure is negative.

Sample size	The sample size determination was described in Ref. 10 (in Methods section, "Differential measurement calculation").
Data exclusions	Not applicable.
Replication	All attempts at replication were successful.
Randomization	Not applicable.
Blinding	Investigators were not blinded to group allocation.

Reporting for specific materials, systems and methods

We require information from authors about some types of materials, experimental systems and methods used in many studies. Here, indicate whether each material, system or method listed is relevant to your study. If you are not sure if a list item applies to your research, read the appropriate section before selecting a response.

Materials & experimental systems

n/a	Involved in the study
☒	☐ Antibodies
☒	☐ Eukaryotic cell lines
☒	☐ Palaeontology
☐	☒ Animals and other organisms
☒	☐ Human research participants
☒	☐ Clinical data

Methods

n/a	Involved in the study
☒	☐ ChIP-seq
☒	☐ Flow cytometry
☒	☐ MRI-based neuroimaging

Animals and other organisms

Policy information about studies involving animals; ARRIVE guidelines recommended for reporting animal research

Laboratory animals	Female Swiss Webster mice (Hsd: ND4, Envigo)
Wild animals	No wild animals were used.
Field-collected samples	No sample was collected from the field for this study.
Ethics oversight	All the laboratory animal protocols were approved by the Institutional Animal Care and Use Committee of California Institute of Technology.

Note that full information on the approval of the study protocol must also be provided in the manuscript.